A comparative spectroscopic study revealing why the CO_2 electroreduction selectivity switches from CO to $HCOO^-$ at Cu-Sn and Cu-In based catalysts

Gumaa A. El-Nagar [a,e], Fan Yang [b+], Sasho Stojkovikj [a,c+], Stefan Mebs [b], Siddharth Gupta [a,c], Ibbi Y. Ahmet [d], Holger Dau[b], Matthew T. Mayer [a,c*]*

[a] Young Investigator Group Electrochemical Conversion of CO_2, Helmholtz-Zentrum Berlin für Materialien und Energie GmbH Hahn-Meitner-Platz 1, Berlin 14109, Germany
[b] Department of Physics, Freie Universität Berlin, Arnimallee 14, Berlin 14195, Germany
[c] Institut für Chemie und Biochemie, Freie Universität Berlin, Arnimallee 22, Berlin D-14195, Germany
[d] Institute for Solar Fuels, Helmholtz-Zentrum Berlin für Materialien und Energie GmbH, Hahn-Meitner-Platz 1, Berlin 14109, Germany
[e] Department of Chemistry, Faculty of Science, Cairo University, Giza 12613, Egypt

Abstract

To address the challenge of selectivity towards single product in Cu-catalyzed electrochemical CO_2 reduction, one strategy is to incorporate a second metal with the goal of tuning catalytic activity via synergy effects. In particular, catalysts based on Cu modified with post-transition metals (Sn or In) are known to reduce CO_2 selectively to either CO or $HCOO^-$ depending on their composition. However, it remains unclear exactly which factors induce this switch in reaction pathways, and whether these two related bimetal combinations follow similar general structure-activity trends. To investigate these questions systematically, Cu-In and Cu-Sn bimetallic catalysts were synthesized across a range of composition ratios and studied in detail. Compositional and morphological control was achieved via a simple electrochemical synthesis approach. A combination of *operando* and *quasi in-situ* spectroscopic techniques, including X-ray photoelectron, X-ray absorption, and Raman spectroscopy, were used to observe the dynamic behaviors of the catalysts' surface structure, composition, speciation, and local environment during CO_2 electrolysis. The two systems exhibited similar selectivity dependency on their surface composition. Cu-rich catalysts produce mainly CO, while Cu-poor catalysts were found to mainly produce HCOO-. Despite these similarities, the speciation of Sn and In at the surface differed from each other, and were found to be strongly dependent on the applied potential and the catalyst composition. For Cu-rich compositions optimized for CO production ($Cu_{85}In_{15}$ and $Cu_{85}Sn_{15}$), indium was present predominantly in reduced metallic form (In^0), whereas tin mainly existed as an oxidized species ($Sn^{2/4+}$). Meanwhile, for the $HCOO^-$-selective compositions ($Cu_{25}In_{75}$ and $Cu_{40}Sn_{60}$), the indium exclusively exhibited In^0 regardless of the applied potential, while the tin resembles was reduced to metallic (Sn^0) only at most negative applied potential, which corresponds to the best $HCOO^-$ selectivity. Furthermore, while $Cu_{40}Sn_{60}$ enhances $HCOO^-$ selectivity by inhibiting H_2 evolution, $Cu_{25}In_{75}$ improves the $HCOO^-$ selectivity at the expense of CO production. Due to these differences, we contend that identical mechanisms cannot be used to explain the behavior of these two bimetallic systems (Cu-In and Cu-Sn). Operando surface-enhanced Raman spectroscopy measurements provide direct evidence of the local alkalization and its impact on the dynamic transformation of oxidized Cu surface species (Cu_2O/CuO) into a mixture of $Cu(OH)_2$ and basic Cu carbonates ($Cu_x(OH)_y(CO_3)_y$) rather than metallic Cu under CO_2 electrolysis. This study provides novel insight into the origin of the switch in selectivity between CO and $HCOO^-$ pathways at Cu bimetallic catalysts and the nature of surface-active sites and key intermediates for both pathways.

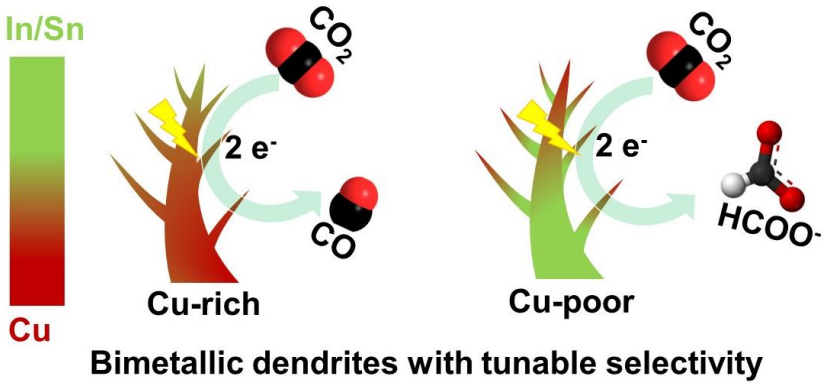

Keywords: CO_2 electroreduction; Cu nanostructures; *In-situ* spectroscopy; Bimetallic catalysts

*Corresponding authors: G. A. El-Nagar (Gumaa.el-nagar@helmholtz-berlin.de) & M. T. Mayer (m.mayer@helmholtz-berlin.de)

+ Equally contributed (shared 2nd authorship)

[e] Permanent address of G. A. El-nagar

1. Introduction

The use of CO_2 as a carbon feedstock will be an important component of a sustainable post-fossil-fuel future. CO_2 can be electrochemically reduced into variety of products including hydrocarbons, alcohols, carbon monoxide (CO) and formate ($HCOO^-$). Recent techno-economic analyses suggest that two-electron reduction of CO_2 into C_1 products (i.e., $HCOO^-$ and CO) presents the best route to economic feasibility in the near future.[1-4] CO and $HCOO^-$ are essential feedstock used in various industrial applications ranging from chemical synthesis (Fisher-Tropsch) to energy conversion (e.g., fuel cells) through existing and emerging technologies.[5-9] The realization of electrochemical synthesis of these important molecules at large scale will require catalysts with high activity and selectivity to the desired products, exceptional stability, sufficient Earth-abundance, and broad availability. New discoveries of improved catalysts, guided by a detailed understanding of structure-activity relationships, are needed in order to progress toward these targets.

The selectivity of CO_2 electroreduction (CO_2ER) is strongly dependent on the nature of the catalyst. Among the single metals which show CO_2ER activity[10], In and Sn are mainly $HCOO^-$ producers, while Cu shows a unique ability to reduce CO_2 into a wide range of products including C_1 compounds (CO, $HCOO^-$ and CH_4) and C_{2+} hydrocarbons (C_2H_4, C_2H_5OH, and others), typically as an undesirable mixture. [6, 11] A variety of approaches, including surface nanostructuring[12-14], and tuning the electronic structure by modifying with a second metal, have been introduced to direct the selectivity of Cu towards a specific product. [11, 15, 16]Several recent studies revealed that modulating the Cu surface with another metal, such as In or Sn, is an effective strategy to tune selectivity towards either CO or $HCOO^-$ at relatively low overpotentials. [17, 18] Luo *et al.* [19], Rasul *et al.* [20] and Zhu *et al*. [18] reported high CO faradaic efficiency (>85% CO FE) at Cu surfaces modified with In nanoparticles. On the other hand, other researchers[18, 21] developed Cu-In bimetallic electrocatalysts with high FE for $HCOO^-$ (>85%). Many other studies revealed a similar behavior for Cu-Sn systems, where researchers reported Cu-Sn catalysts with high FE towards either CO or $HCOO^-$. [9, 17, 22] For instance, Li *et al.* [23] investigated CO_2ER on Cu/SnO_2 core-shell nanoparticles with various Sn shell thickness, finding the selectivity to strongly depend on said thickness, with thicker Sn shells showing Sn-like activity with high $HCOO^-$ selectivity (FE ~90%), while thinner shell exhibited a high CO selectivity (FE ~93%). Moreover, our recently published work[17] reported a similar behavior for Cu nanowires coated with ultrathin SnO_x layers grown using atomic layer deposition, and detailed X-ray spectroscopic investigation revealed differing Sn speciation (i.e. oxidation state) between the CO- and $HCOO^-$-selective catalysts.

In those previous studies, the general trend is that Cu-In and Cu-Sn catalysts with low In and Sn contents (Cu-rich catalysts) are CO-selective, while those with high Sn and In contents (Cu-poor catalysts) showed a higher tendency toward $HCOO^-$. A variety of mechanistic hypotheses, such as alloying and electronic effects, have been proposed to explain these bimetallic synergetic effects, mostly centered around the crucial role of Cu-In and Cu-Sn interfaces in tuning the binding strength of the key intermediates (e.g., *COOH, *OCHO and *H) and consequently, CO and $HCOO^-$ selectivity. [17, 19, 23-25]For instance, DFT calculations attribute the selectivity shifts (from CO to formate) with increasing of In or Sn contents to the gradual weakening of the adsorbed *COOH intermediate (which leads to CO), concurrently with enhancing the adsorption of *OCHO intermediate (resulting in $HCOO^-$). A plausible explanation of this observed shift from carbophilic (*COOH, C-bound) to oxophilic (*OCHO, O-bound) adsorption modes could be the charge transfer from Sn or In to Cu sites resulting in localized positive charge regions. These regions on the catalyst surface hamper the adsorption of *COOH intermediate and hence increases the competitiveness of the $HCOO^-$ production pathway at the expense of the CO formation pathway. [18, 24] These theoretical investigations on Cu-In and Cu-Sn suggest a direct correlation between the surface atomic environment (surface composition) and the surface electronic properties (charge distribution) and indicate their essential inextricable role to the binding energy of the key intermediates for CO and $HCOO^-$ production.

The surface composition and speciation of Cu-based bimetallic catalysts (Cu-Sn and Cu-In) have substantial effects on their performance (selectivity) for CO_2ER, as discussed above. However, most of the previous studies build their mechanistic hypotheses based on structural information gathered from *ex-situ* measurements conducted either before or after CO_2ER testing. Since it is well known that catalyst materials can significantly transform under CO_2ER measurement conditions, basing DFT calculations on such structural information as a main way to explain the observed selectivity trends of these bimetallic systems can be challenging and potentially misleading, as the models likely do not represent the precise active-surface species. Accordingly, in-depth exploration of the surface chemical environment, speciation (oxidation states), structure and composition

of those bimetallic systems using combination of appropriate and complementary surface-sensitive techniques via operando/*in-situ* configurations is required to fully expose the complex link between their composition, intermediate adsorption, and selectivity. As mentioned above, limited number of studies have reported the high selectivity of Cu-In catalysts into either CO or $HCOO^-$, but none of them, to the best of our knowledge, provide detailed insight into the active surface speciation. Furthermore, while one may presume that Cu-In and Cu-Sn systems follow the same mechanisms for selectivity tuning based on the similar composition–activity trends, to date no study has systematically compared the two to address this possibility. Thus, there is a need for detailed and systematic investigations of the surface properties of such bimetallic catalysts to define the precise surface-active species, which govern their selectivity shift from CO to $HCOO^-$.

This work is mainly dedicated to provide a thorough structure-composition-activity comparison between Cu-In and Cu-Sn bimetallic electrocatalysts using various surface and bulk sensitive X-ray spectroscopic techniques, aimed at providing insight into the open questions regarding the similarity and differences between those two systems. In this regard, multiple complementary techniques including quasi *in-situ* X-ray photoelectron spectroscopy (XPS) and X-ray absorption spectroscopy (XAS) combined with *in-situ* surface enhanced Raman spectroscopy (SERS) were used to probe the chemical environment and surface changes under CO_2ER electrolysis. A simple one-pot electrochemical synthesis strategy was used to prepare bimetallic Cu-In and Cu-Sn with dendrite-like structures across a range of controlled In and Sn contents to tune their selectivity towards either CO or HCOO-. *In-situ* SERS was used to probe the catalyst/electrolyte interface changes (e.g., local pH changes, surface oxide species) and key intermediates of CO_2 reduction for a better understanding of the origin of the preference shift from C-bound intermediate to O-bound intermediate with increase of Sn/In surface contents. This comparative study highlights key differences in the surface composition and speciation (surface-active species) between Cu-In and Cu-Sn bimetallic systems under CO_2 electroreduction conditions, despite both systems showing similar CO_2ER catalytic activity behaviors. It also introduces new insights into the debated role of the persistence metal surface oxide species and their dynamic transformations during CO_2ER.

2. Experimental

Cu-Sn and Cu-In nanostructures of various compositions were grown onto Cu mesh substrates using a simple electrodeposition approach. In brief, Cu was co-electrodeposited simultaneously with either In (to create Cu-In) or Sn (to fabricate Cu-Sn) from 1.5 M H_2SO_4 solutions containing Cu/In or Cu/Sn salts at different molar ratios via applying relatively high cathodic current (1 A/cm^2). Under these conditions, H_2 bubbles generated *in-situ* act as a dynamic template for constructing foam-like structures with mesoscale porosity. The morphology, structure and composition of the as-prepared bimetallic materials were examined by various material characterization techniques. *In-situ* SERS and glovebox-assisted XAS and XPS were used for tracking dynamic changes of CO_2ER intermediates and local changes of bimetallic surfaces and environment under CO_2ER conditions. Gaseous and liquid products were quantified via gas chromatography and high-performance liquid chromatography. Comprehensive details of the materials, synthesis procedures and characterization methods are provided in the supplementary information.

3. Results and Discussion

3.1 Material characterization

The physical properties, including morphology, thickness, porosity, crystalline structure, and surface/bulk compositions, of the as-prepared Cu_xSn_y (x = at. % Cu, y = at.% Sn) and Cu_xIn_z (z = at.% In) bimetallic catalysts were first evaluated using different material characterization techniques. As shown in **Figure 1** and **Figure S1-2**, porous Cu-Sn and Cu-In bimetallic foams with a range of compositions (various In and Sn contents) were successfully synthesized through a one-step co-electrodeposition synthesis approach, **as described in experimental section in SI**. While the resulting materials exhibited similar dendrite-like microstructures, the fine microstructure of these dendrites showed some variation dependent on the Cu/In and Cu/Sn molar ratios in the deposition solution (**see Figure S1-2**). The shape of these electrodeposited dendrites is mainly controlled by the rate of metal deposition and the rate of the concurrent hydrogen evolution reaction. The presence of either In or Sn in the Cu deposition bath is seen to have a significant impact on the nucleation, growth and

break-off rates of the *in-situ* generated hydrogen bubbles, and hence on the fine structure and physical properties (e.g., porosity, thickness, *etc*) of the obtained porous foams[21]. The presence of Cu as foaming agent is essential to create these dendritic microstructures (porous foams), since the fabricated pure Sn and In did not show any dendrite-like structures. Contrary to the mixed metal depositions, electrodeposition from solutions of only Sn resulted in porous Sn thin films composed of interconnected Sn tubes (fishbone-like structures, **Figure S1**), while pure In exhibited a rough thin layer composed of In grains (**Figure S2**).

Grazing incidence X-ray diffraction (GI-XRD) was next used to examine the crystalline structures of the as-prepared foams, data are displayed in **Figure 2**. Pure Cu foam exhibited mainly the typical reflection peaks for cubic metallic copper with a small contribution from Cu_2O, while the various as-prepared Cu-Sn bimetallic foams showed a mixture of metallic copper and Cu_2O phases. Additionally, the pure electrodeposited Sn exhibited several reflection peaks attributed to metallic Sn. No significant shifts are observed in the Cu reflection peaks of the all as-synthesized Cu-Sn foams compared to pure Cu. The foams with low Sn contents did not exhibit any noticeable signal for Sn (metallic or oxide), suggesting the electrodeposited Sn exists in an amorphous state or is below the detection threshold for XRD. Taken together, there is no clear evidence of the formation of crystalline Cu-Sn alloys. Cu-In bimetallic foams with low In content (≤48 at. %) exhibited mainly reflection peaks for the metallic copper with small contribution of metallic In, while Cu-In foams with higher In contents beyond 48 at. % displayed a mixture of metallic In and Cu.

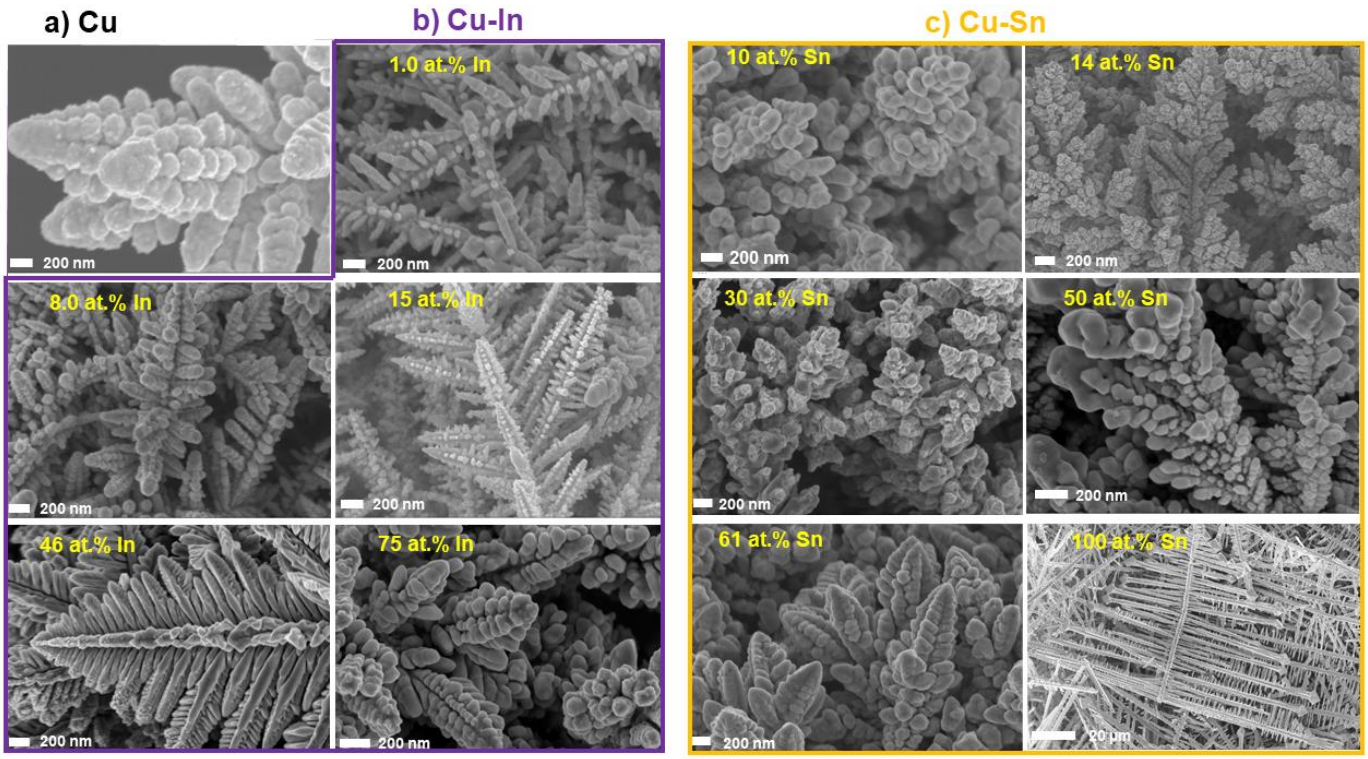

Figure 1. Representative SEM images of pure Cu (a) and bimetallic Cu-In (b, violet border) and Cu-Sn (c, orange border) dendrites with various In and Sn contents. In and Sn atomic percentages (at.%) are provided in the SEM images as estimated from their respective EDX analysis.

Again, the as-prepared Cu-In bimetallic foams did not show evidence of crystalline Cu-In alloy formation. It is worth noting that, while the Cu-rich Cu-Sn foams exhibited very strong peaks for Cu_2O with very low contribution of metallic Cu, the Cu-rich Cu-In foams showed only metallic Cu reflections. However, as described later in section 3.3, XAS measurements under CO_2 electrolysis conditions suggest the formation of Cu-In and Cu-Sn alloys, in addition to the existence of In and Sn oxides (see section 3.3 for more details). Furthermore, XPS (more surface-sensitive) analyses of these samples (air-exposed), showed the existence of a thin surface oxide shell for all the as-prepared Cu-In and Cu-Sn bimetallic catalysts (**see Figure S3**). We only measured XAS and

XPS for the Cu-In and Cu-Sn bimetallic foams with the best CO_2ER performance towards either CO or $HCOO^-$.

3.2 CO_2 electroreduction performance

The electrochemical CO_2 reduction performance of the various as-prepared Cu-In and Cu-Sn bimetallic foams with a wide range of compositions was examined in CO_2-saturated 0.1 M $KHCO_3$ using a two compartment, three-electrode H-type electrochemical cell. The obtained CO_2ER performance results are summarized in **Figure 3 and Figures S4-6**. **Figure 3** displays the faradaic efficiency of CO and $HCOO^-$ formation as function of Sn and In contents at various applied cathodic potentials. A similar trend in selectivity towards CO and $HCOO^-$ pathways is observed for both the bimetallic foam systems, wherein Cu-rich bimetallic (Cu-In and Cu-Sn) foams showed a high CO-selectivity, while Cu-poor foams exhibited a high tendency towards $HCOO^-$ production. Even introducing trace amounts (≤1.5 at.%) of either Sn or In into Cu foam, shifts its selectivity significantly towards CO production, and Sn or In contents of approximately 15 at.% resulted in peak CO selectivity reaching above 90 %. Further increase in either metal results in an abrupt decrease of CO selectivity. Hereafter, $Cu_{85}In_{15}$ and $Cu_{85}Sn_{15}$, representing the foams with the highest CO-selectivity, will be used for further detailed investigation. It is worth mentioning here that $Cu_{85}In_{15}$ foam exhibited its highest FE for CO of ~92% at -0.6 V RHE, while $Cu_{85}Sn_{15}$ achieved a similar FE for CO but at more negative potential (-0.7 V RHE).

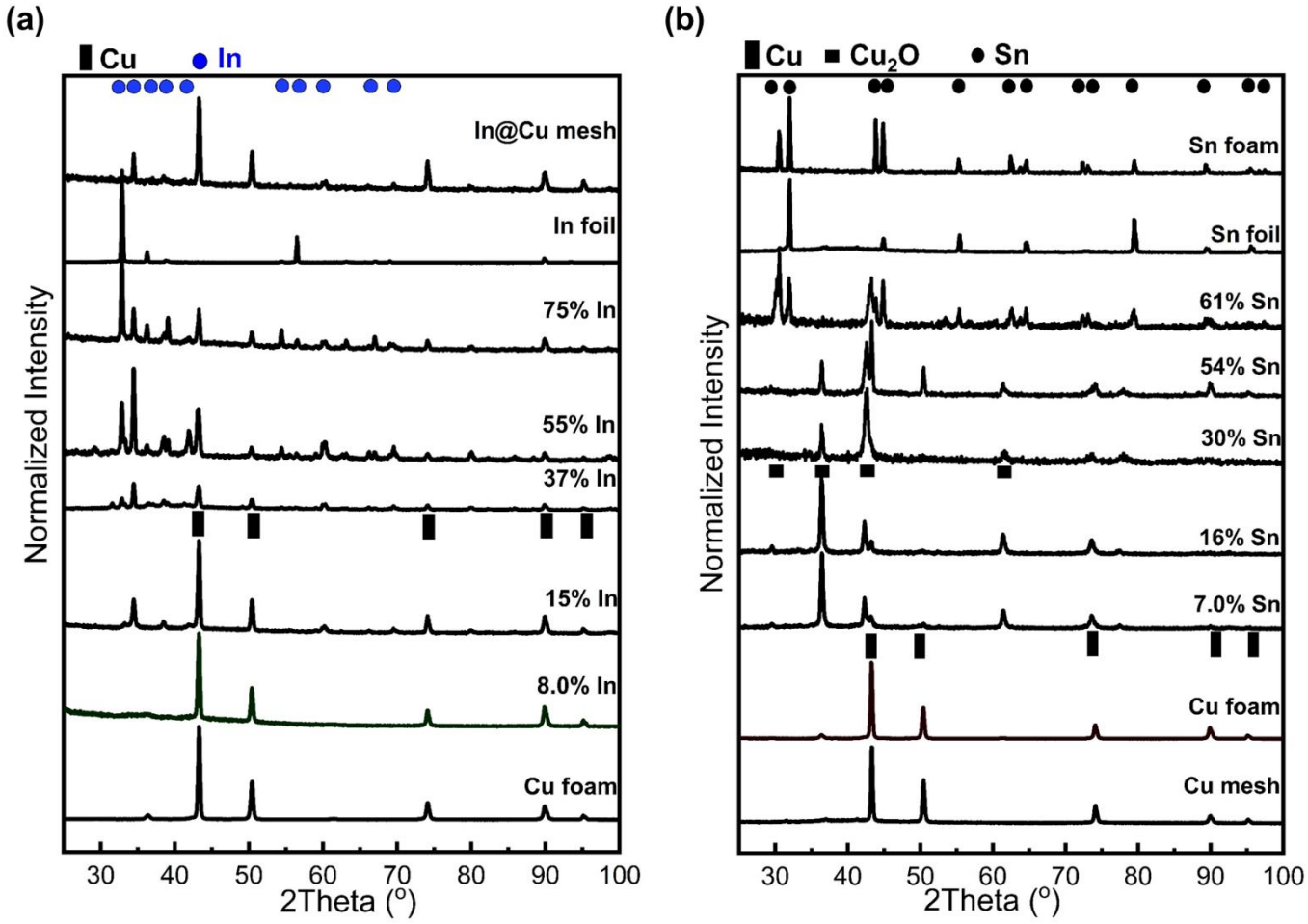

Figure 2. Representative XRD patterns of some selected as-prepared Cu-In (a) and Cu-Sn (b) bimetallic foams with various Sn and In contents, respectively, deposited onto Cu mesh substrates. The labeled In and Sn contents are obtained from their respective EDX analysis. Symbols are used to indicate peaks attributable to the phases mentioned in the legend, at peak positions derived from reference patterns for each material.

Further increase of the Sn and In contents lead to steadily increasing $HCOO^-$ selectivity, plateauing for contents above 50-60 at. %, accompanied by greatly suppressed CO yields. $Cu_{40}Sn_{60}$ and $Cu_{25}In_{75}$ will be used henceforth for indicating the foams with the highest $HCOO^-$ selectivity. Both displayed the best $HCOO^-$ selectivity at -0.9 V RHE. Further detailed studies were only performed on the Cu-In and Cu-Sn foams with the best selectivity towards CO ($Cu_{85}In_{15}$ and $Cu_{85}Sn_{15}$) and $HCOO^-$ ($Cu_{40}Sn_{60}$ and $Cu_{25}In_{75}$). Furthermore, **Figure S4** shows the distribution of FE for H_2 as a function of Sn and In contents (at. %) at various applied cathodic potentials. As shown in this figure, the selectivity of the competitive undesired hydrogen evolution reaction is significantly suppressed upon modifying Cu foams with even small amounts of either In or Sn.

Figure 4, Figure S5 and S6 display the distribution of faradaic efficiencies (FEs) and partial current densities of the different major products obtained at Cu-Sn and Cu-In bimetallic foams optimal for CO and $HCOO^-$ production compared to their respective single elements at various applied cathodic potentials. $Cu_{25}In_{75}$ and $Cu_{40}Sn_{60}$ showed a similar steady increase of the $HCOO^-$ selectivity with the increase of the applied potential (**Figures 4a and 4b**), however they exhibited quite different selectivity trends for CO and H_2. $Cu_{25}In_{75}$ showed low H_2-selectivity with high CO-selectivity at low potentials, while $Cu_{40}Sn_{60}$ in contrast exhibited high H_2-selectivity with very low CO-selectivity under similar conditions. On the other hand, the Cu-rich Cu-Sn and Cu-In bimetallic foams ($Cu_{85}In_{15}$ and $Cu_{85}Sn_{15}$) exhibited a kind of similar volcano-shaped trend for the CO selectivity with maximum at -0.6 V and -0.7 V vs. RHE (all potentials given herein are relative to the RHE) for $Cu_{85}In_{15}$ and $Cu_{85}Sn_{15}$, respectively. Despite their similar CO selectivity behavior, they showed differences in the H_2 formation behavior. $Cu_{85}Sn_{15}$ foam showed a high tendency for H_2 production at low potentials (<-0.6 V), while $Cu_{85}In_{15}$ exhibited a high CO selectivity (>50% CO FE) even at relatively lower overpotential (-0.4 V). The pure Sn and In catalysts followed similar CO, H_2 and $HCOO^-$ trends, where the $HCOO^-$ selectivity increases with the potential accompanied with decrease of both H_2 and CO production. However, the pure In still shows higher CO and lower H_2 selectivity at less negative potentials compared to the pure Sn.

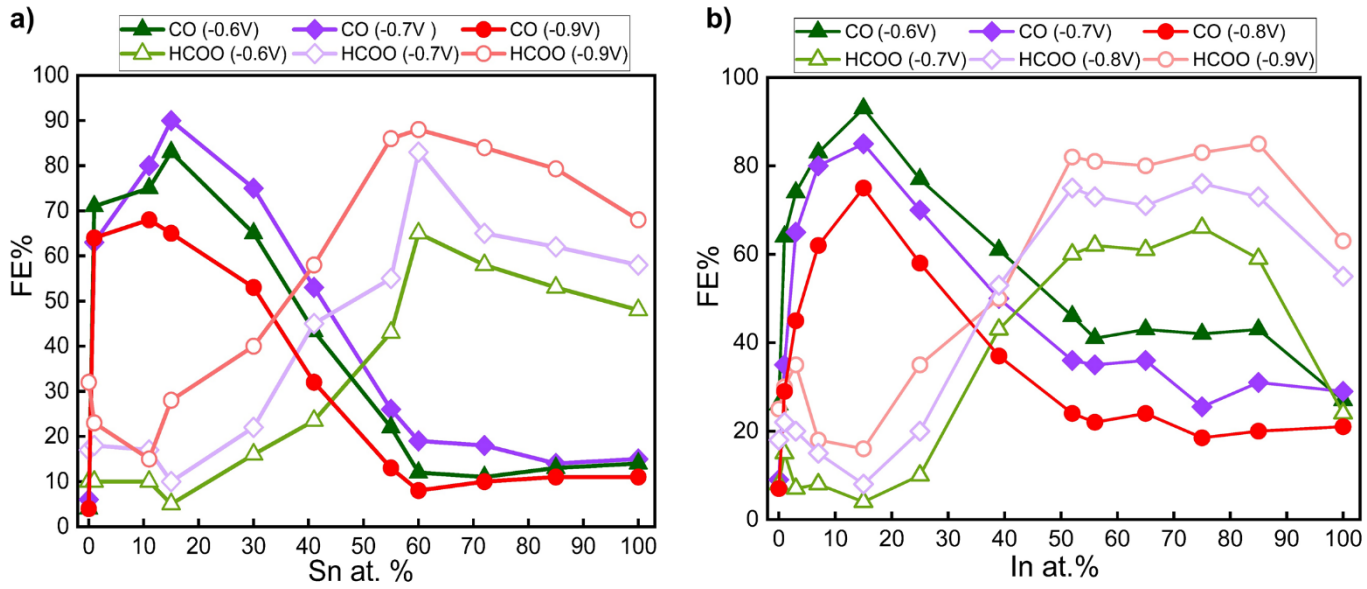

Figure 3. Distribution of CO and $HCOO^-$ FE for Cu-Sn (a) and Cu-In (b) bimetallic foams as a function of Sn and In contents at several applied cathodic potentials. Each different x-axis value represents a separately prepared sample of different composition, tested at a range of potentials (indicated by different symbols/colors) and reporting the FE towards the major products CO (solid symbols) and HCOO- (hollow symbols). The yields of H_2 and other minor products are omitted for clarity.

More thorough analysis of the physical properties (e.g., porosity, thickness and roughness) of the Cu-In and Cu-Sn bimetallic foams with the best CO and $HCOO^-$ selectivity is essential for better understanding the wide variance in the observed currents and selectivity. Thus, the thickness and porosity of these bimetallic foams were estimated from their respective cross-section FIB-SEM (see **Figure S7**). Their roughness, bulk and surface compositions were estimated using XPS (**Figure S3**), EDX (**Figure S8-9**) and ICP-OES, obtained results summarized in Table 1.

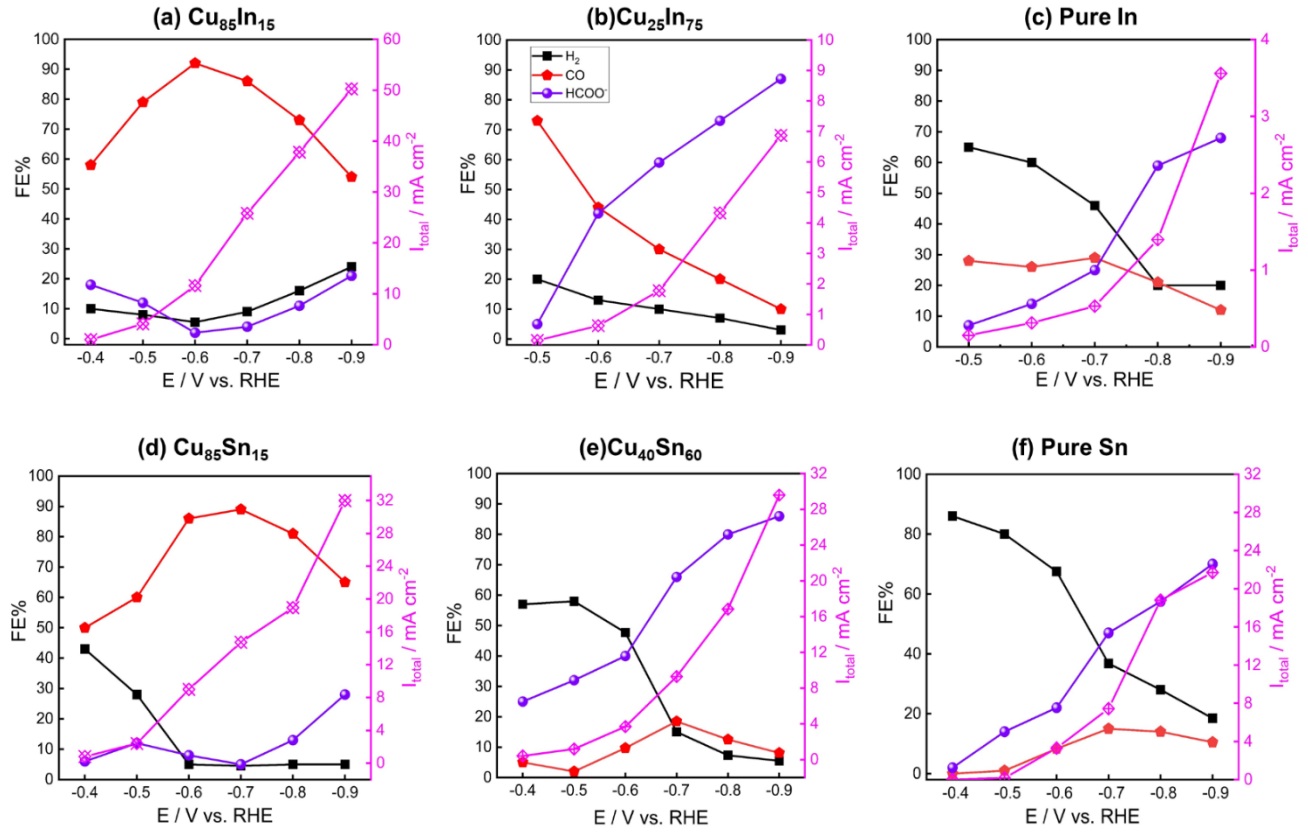

Figure 4. Potential-dependent faradaic efficiency distribution of major products (CO, $HCOO^-$ and H_2) and the obtained total current (I_{total}, right y-axes) for bimetallic foam catalysts optimal for CO production ((a) $Cu_{85}In_{15}$ and (d) $Cu_{85}Sn_{15}$) and $HCOO^-$ production ((b) $Cu_{25}In_{75}$ and (e) $Cu_{40}Sn_{60}$), compared to (c) pure In and (f) pure Sn.

Table 1. A summary of the various physical parameters including roughness, thickness, pore-size and morphology, in addition to the bulk and surface composition of the as-synthesized bimetallic dendrites.

Catalyst	Cu/M (M=Sn or In) composition ratio		Roughness*	Thickness (µm)	Average Pore size (µm)	Morphology	Major product
	XPS (surface)	ICP-OES (bulk)					
Cu	N/A	N/A	173	64	28	Foam/dendrites	H_2 & C2+ products
$Cu_{85}In_{15}$	3.4	3.8	156	40	25	Foam/dendrites	92% CO
$Cu_{85}Sn_{15}$	5.0	3.3	540	52	30	Foam/dendrites	90% CO
$Cu_{25}In_{75}$	1.0	1.1	73	14	25	Foam/dendrites	86% $HCOO^-$
$Cu_{40}Sn_{60}$	0.04	0.02	204	16	36	Foam/dendrites	87% $HCOO^-$
Sn	N/A	N/A	320	N/A	N/A	Foam/Fishbone-like structures	70% $HCOO^-$
In	N/A	N/A	10	N/A	N/A	Rough-porous layer	62% $HCOO^-$

* Estimated by dividing C_{dl} of bimetallic by C_{dl} of Cu mesh

Additionally, their electrochemically active surface area (roughness) was estimated via measurement of capacitive double layer behavior, as shown in **Figure S10.** Despite $Cu_{85}In_{15}$ (CO-selective) showing significantly lower electrochemically active surface area (see Table 1) compared to $Cu_{85}Sn_{15}$ (CO-selective), it exhibited higher CO_2ER total current (Figure S5b). This indicates the higher intrinsic activity and the superiority of $Cu_{85}In_{15}$ over $Cu_{85}Sn_{15}$. In contrast, $Cu_{40}Sn_{60}$ (HCOO-selective, Figure S6b) showed higher CO_2ER current compared to the $Cu_{25}In_{75}$ (Figure S5c) which could be attributed to its significantly higher electrochemically active surface area. So far, we have succeeded in fabricating and fully characterizing the Cu-In and Cu-Sn bimetallic dendrites with tunable performance towards either CO (Cu-rich dendrites) or $HCOO^-$ (Cu-poor dendrites) production. The improved CO and $HCOO^-$ selectivity on the bimetallic dendrites cannot be attributed to the alloying effect, since the obtained XRD patterns did not exhibit any signs for the existence of a crystalline alloy. Both bimetallic systems (Cu-In and Cu-Sn) showed a similar CO and HCOO- selectivity-dependence on In and Sn contents, where their $HCOO^-$ selectivity increases with the applied potential with a simultaneous decrease in their tendency to produce CO. Despite their CO and $HCOO^-$ selectivity trends, their enhanced ability to yield CO and $HCOO^-$ could be attributed to different enhancing mechanisms. $Cu_{25}In_{75}$ showed a kind of linear increase of $HCOO^-$ selectivity at the expense of CO, while $Cu_{40}Sn_{60}$ seems to enhance the $HCOO^-$ selectivity at expense of H_2 production. Although the above *ex situ* characterization provides insight into the observed selectivity trends, it is known that electrocatalysts can transform significantly during electrochemical operation, and transition metals in particular can be susceptible to oxidation in air during post-run sample handling. A more precise understanding of the true catalytic interface requires the use of *in situ* methods capable of characterizing the operating system. Thus, quasi *in-situ* XPS and XAS together with operando SERS were next used to examine the induced local environment (local pH) and surface (speciation and composition) changes during CO_2 electroreduction at both bimetallic systems.

Quasi In-situ XPS and XAS measurements

A so-called quasi *in-situ* XPS approach was used to explore the surface composition and speciation of the bimetallic systems giving the best CO and $HCOO^-$ performance. CO_2 electrolysis was carried out at various potentials in an O_2-free glovebox under inert (N_2) atmosphere. Then, the measured samples were rapidly transferred to the XPS analysis chamber under vacuum without any air exposure through a gastight transfer capsule. In this way, we sought to avoid the re-oxidation of the tested catalysts' surfaces, providing chemical and compositional insight more representative of their real surface-active species. The quasi *in-situ* XPS results are summarized in **Figure 5-6** and **Figure S11-13**. Immediately noticeable is that while the surface of the different as-prepared bimetallic foams and their single-metal counterparts (Cu, Sn and In) are mostly dominated by oxide species (e.g., Cu_xO_y, SnO_x and In_xO_y) (**Figure S3**), the samples measured after electrocatalysis have distinctly transformed surface speciation.

General observations based on our evaluation of the obtained Cu 2p spectra (see **Figure S11 and Figure S3**), and Cu LMM Auger regions (see **Figure 5, Figure S13 and Figure S4**) are:

(I) Before CO_2ER, the surface of all the as-synthesized materials, CO and $HCOO^-$ selective bimetallic foams, is predominated by Cu^+ species (≥65%) with a small contribution from metallic Cu (≤20%) and Cu^{2+} (~25%). It is worth mentioning here that some of the as-synthesized catalyst compositions ($Cu_{85}In_{15}$, $Cu_{25}In_{75}$ and $Cu_{40}Sn_{60}$) did not display any Cu^{2+} surface species, but exhibited mainly Cu^+ species with a low metallic copper contribution, **Figure S3 and Figure S11**.

(II) A complete transformation of the different detected surface copper oxide species (Cu^{2+} and Cu^+) into metallic copper was observed for all investigated catalyst materials (i.e., Cu, Cu-In and Cu-Sn foams) following CO_2ER in the glovebox and the subsequent transfer to the XPS under an inert atmosphere. This was true regardless of the applied cathodic potential (-0.5 V to –0.9 V) and the different bimetallic compositions studied. Additionally, brief exposure of any of these catalysts to air resulted in significant re-oxidation of their surface into various copper oxide species (Cu^+ and Cu^{2+}) with small contribution of metallic copper, as shown in **Figure 5 and Figures S11-12**.

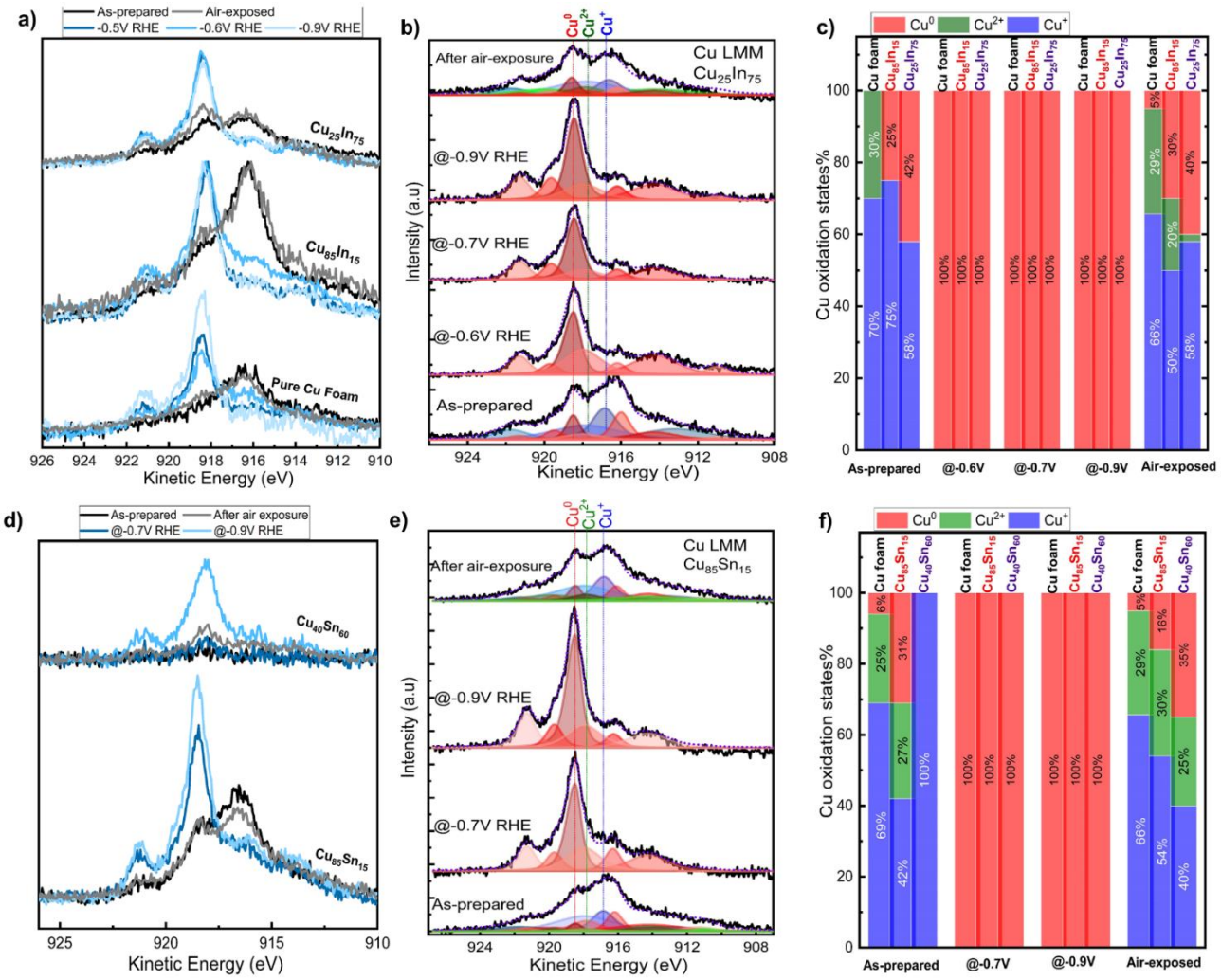

Figure 5. Quasi *in-situ* XPS for copper speciation based on Cu LMM Auger analysis. Summary of raw data (left column), representative peak fittings (middle), and fitting results (right) for Cu-In (a-c) and Cu-Sn (d-f) bimetallic foams following different ambient or electrochemical conditions.

The Cu LMM Auger analysis revealed the surface transformation to metallic Cu^0 without any detectable residual oxides following electrocatalysis, and furthermore shows how the as-prepared materials as well as the post-electrolysis samples exposed to air undergo significant surface oxidation. Taken together, these observations help validate the usefulness of the quasi in situ XPS approach and highlight the limitations of using *ex situ* approaches to study electrocatalyst surfaces. The obtained Cu results emphases the existence of mixed heterogeneous surface of separate metals, rather than alloying since we did not detect any meaningful shift of the Cu 2p spectra of the bimetallic systems compared to the Cu 2p of pure Cu. Unlike the Cu surface species, the analysis of the In 3d and Sn 3d spectra of bimetallic foams showed that the identified In and Sn surface species are strongly dependent on the initial composition and the applied potentials (**Figure 6**). CO selective bimetallic foams (Cu-rich, $Cu_{85}In_{15}$ and $Cu_{85}Sn_{15}$) showed different surface speciation compared to $HCOO^-$ selective catalysts (Cu-poor, $Cu_{25}In_{75}$ and $Cu_{40}Sn_{60}$). Before CO_2 electrolysis, CO selective bimetallic foams, as well as their respective single elements (In and Sn) exhibited nearly fully oxidized In and Sn surface species with a tiny contribution (<4%) of metallic species (In^0 and Sn^0). Looking first at the Cu-In catalysts (**Figure 6a-d**), we see that after CO_2 electrolysis at -0.5 V (or more negative potentials), the oxidized In surface of the pure In and $Cu_{85}In_{15}$ catalysts is severely reduced, where the quantification of their surfaces revealed the predominance of metallic In (77-86% In^0) with a small contribution of oxidized In species (23-14% In^{n+}).

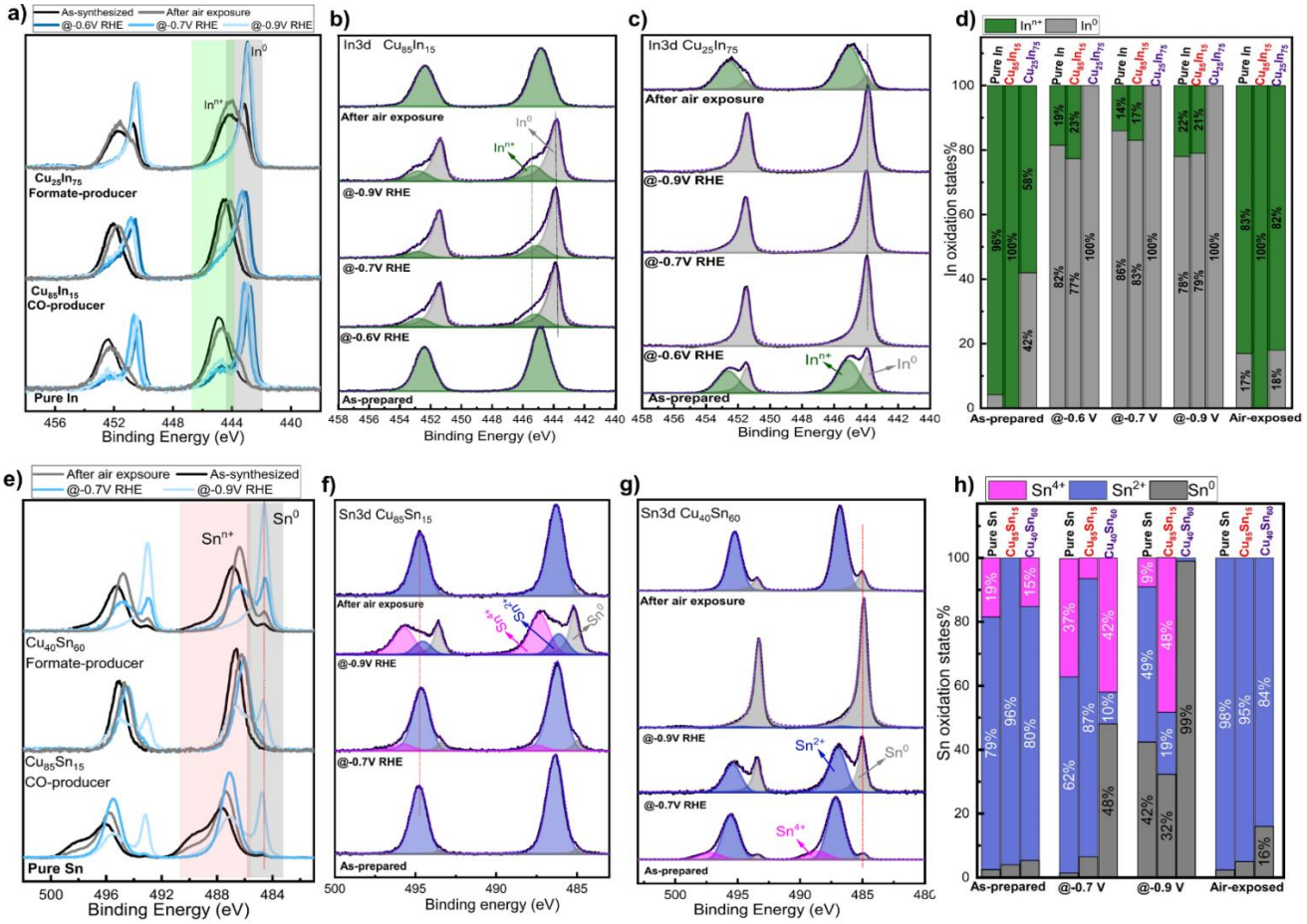

Figure 6. Quasi *in-situ* XPS results of In3d (a-d) and Sn3d (e-h) of Cu-In and Cu-Sn bimetallic dendrites. Overlay of the obtained In3d (a) and Sn3d (e) of the Cu-In and Cu-Sn bimetallic foams at various applied potentials without fittings. Summary of In and Sn surface oxidation states and representative fittings and of In3d and Sn3d spectra of Cu-In (a-d) and Cu-Sn (e-h) bimetallic foams with best CO and $HCOO^-$ performances, respectively.

On the other hand, $Cu_{25}In_{75}$ ($HCOO^-$ selective catalysts) exhibited a mixture of metallic (58% In^0) and oxide (42% In^{n+}) In surface species before CO_2ER. Interestingly, $Cu_{25}In_{75}$ exhibited exclusively metallic In after CO_2 electrolysis at all the studied potentials (-0.5 V to -0.9 V RHE). In summary, the obtained XPS results of Cu-In bimetallic foams reveal that the active surface of $Cu_{85}In_{15}$ foam is composed of metallic Cu^0 and mixture of metallic In^0 (predominant species) and oxidized In (In^{n+}), while $HCOO^-$ selective $Cu_{25}In_{75}$ surface is exclusively composed of Cu^0 and In^0.

The quantification of Sn surface speciation of CO and $HCOO^-$ selective Cu-Sn bimetallic dendrites (**Figure 6e-h**) displayed substantial differences compared to the Cu-In bimetallic dendrites under similar measuring conditions. Before CO_2ER, the surface of the as-synthesized pure Sn, $Cu_{85}Sn_{15}$ and $Cu_{40}Sn_{60}$ foams exhibited predominantly oxidized Sn (~95% Sn^{n+}) with a residual of metallic Sn (Sn^0). After CO_2ER at -0.7 V, no major changes were detected in Sn surface specification of $Cu_{85}Sn_{15}$ (CO selective) catalysts, where their surfaces are predominantly composed of oxidized Sn species (~87% Sn^{2+} and 7% Sn^{4+}). Interestingly, at -0.9 V RHE the Sn^{2+} gave way to significant increases of Sn^0 and Sn^{4+} species. On the other side, $HCOO^-$ selective Cu-Sn sample ($Cu_{40}Sn_{60}$) showed a great increase in the metallic Sn contents after CO_2 electrolysis at -0.7 V RHE and -0.9V RHE, where Sn^0 increased from 4% before CO_2ER into 48% and ~100% at -0.7 V and -0.9 V, respectively. Additionally, the brief air exposure of any of these catalysts leads to a near complete re-oxidation of their surfaces, highlighting again the effectiveness of using glovebox assisted XPS for identifying the surface-active species. **Figure S14** summarizes surface composition and speciation of the all investigated electrodes including CO selective and $HCOO^-$ selective bimetallic Cu-In and Cu-Sn foams.

A closer look at the surface speciation of these two $HCOO^-$ selective bimetallic systems ($Cu_{25}In_{75}$ and $Cu_{40}Sn_{60}$) reveals the fully metallic nature of all elements at the potential with the best $HCOO^-$ production (-0.9 V). Despite their similar speciation and CO_2ER performance at -0.9 V, they displayed a completely different CO_2ER behavior at lower potentials (see **Figure 4a and 4b**), with $Cu_{25}In_{75}$ yielding mainly CO at low potentials (<-0.7 V) while $Cu_{40}Sn_{60}$ produces mostly H_2. These differences in the major products at low potentials may originate from the differences in their surface speciation (**Figure 6 and Figure S14**). Where the fully metallic surface of $Cu_{25}In_{75}$ seems to have a high tendency for CO production with little H_2 formation, partially oxidized Sn surface of $Cu_{40}Sn_{60}$ favored H_2 production over CO at low potentials. Scheme 1&2 summarize the surface-active species of CO- and HCOO-selective bimetallic catalysts, as evaluated from quasi *in-situ* XPS, and depict our theory of how they are related to the observed selectivity switch from CO for Cu-rich to HCOO- for Cu-poor bimetallic catalysts. The enhanced CO-production at Cu-rich system can be attributed to the localized partial negative charge on Cu sites due to the charge transfer from Sn/In atoms to Cu. This charge transfer from Sn/In into Cu led to partial positive charge on Sn/In atoms, indicated by the oxidized Sn and In species, and hence stabilizing the *COOH intermediate (CO-pathway). [17, 24] Within the resolution of our XPS analysis we do not observe clear evidence of charge transfer, but rather both metals are fully reduced on the surface. Thus, Cu-poor catalysts (HCOO-selective) is thought to enhance the HCOO-pathway by inhibiting the H-adsorption and stabilizing the *OCHO intermediate (HCOO-pathway), see *in-situ* SERS below.

Bulk-sensitive XAS measurements were conducted for a set of 16 quasi *in-situ* samples in order to complement the surface-sensitive XPS measurements. [26] The X-ray absorption near-edge structure (XANES) provides estimates for the oxidation state – particularly the contribution of oxide phases – as well as the local geometry around the X-ray absorbing atom. The extended X-ray absorption fine-structure (EXAFS) is determined by backscattering of the electron-wave created at the X-ray absorbing atom; it provides bond distances and coordination numbers of the backscattering atoms in the first 3-5 coordination shells around the X-ray absorbing atom. Since XAS of (inter)metallic phases such as alloys tend to suffer from reabsorption effects and show very strong FT amplitudes for the metallic back scatterers, potentially hiding shells of lighter atoms (e.g., oxygen) or low amounts of other atoms (e.g., In or Sn), efforts have been made in careful data evaluation and thoroughly modeling the data, resulting in a total of almost 180 fit models in EXAFS (see SI for details). With this comprehensive approach, we address the following (interrelated) questions from the XAS-perspective:

(i) Are the metal atoms in the reduced Cu-In/Sn materials present as alloys or separate metallic phases? (ii) What are the Cu/In or Cu/Sn stoichiometries in the alloy phase?
(iii) What is the level of crystallinity? What are the metal oxidation states and oxidic contributions?
(iv) What is the effect of the applied potentials? Are In or Sn leaching or enriching during operation?

We modeled the EXAFS data with and without In or Sn shells and with or without multiple-scattering (MS) shells, the latter providing information on the level of crystallinity. For the intermetallic Cu-In and Cu-Sn samples, this resulted in 13 fit models each. A subsequent meta-analysis of R-values, first-shell distances, and populations, and Cu/In or Cu/Sn ratios disclosed the superior models, which are presented here.

Figures 7 a-d display Cu-, In-, and Sn-XANES of Cu-In and Cu-Sn Cu-rich samples for different potentials. Spectra of metallic foils, typical oxides, and reduced Cu-foam for Cu-XANES, are given as references. First glance inspection of the Cu-XANES immediately hints towards three aspects, in that (1) the Cu-In and Cu-Sn spectra are neither looking like Cu-foil, Cu_2O nor pure reduced Cu-foam (**Figure S15**), but are also not just a superposition of those (**Figures S16-S18**, **Tables S1-S7**), which is due to the presence of In or Sn atoms within the Cu-phase; (2) oxidations states of Cu are close to zero (a quantification was attempted but is largely excluded due to the lack of proper references, see Table S8 for details); and (3) there are only minor responses against applied potentials, which may include the reduction of low amounts of (surface) oxidic species. To the contrary, pronounced changes are obtained for the In- and Sn-XANES. Notably, In-XANES of the Cu-In samples can indeed be well approximated as a linear combination[27] of In-foil and In_2O_3, and the as-prepared samples basically resemble In_2O_3 (**Figures 7c and S23**), suggesting not only strong oxidic contributions, but in addition the formation of a separate In-phase. After application of reducing potentials, the spectra indicate significant reduction and get very close to the In-foil spectra. Linear combination techniques indicate almost 100% In_2O_3

content for $Cu_{85}In_{15}$ (Cu-rich) as-prepared samples and a ratio of about 85:15 (In^{2+} : In^0) for $Cu_{25}In_{75}$ (Cu-poor) as-prepared samples (Table S4). To the contrary, as-prepared Sn-spectra of Cu-Sn samples can only be modeled by superposition of Sn-foil, and SnO_2 (instead of SnO, Figure S24 and Table S5), with ratios of about 36:64 ($Sn:SnO_2$) for as-prepared $Cu_{40}Sn_{60}$ samples and 49:50 for as-prepared $Cu_{85}Sn_{15}$ samples, hinting towards an average oxidation state around 2 for Sn. Whereas little to no response to applied potentials was observed for the Sn-edge in $Cu_{85}Sn_{15}$ (Figure S22e), the oxide-to-foil-trend obtained for the Sn-spectra is also visible for the Cu-poor case ($Cu_{40}Sn_{60}$, Figure S22f), which again suggests that most of the Sn atoms are incorporated into the Cu-phase for the Cu-rich case ($Cu_{85}Sn_{15}$), but a separate Sn(Ox)-phase might have formed for the Cu-poor case ($Cu_{40}Sn_{60}$).

The XANES results are supported by the Cu-EXAFS results. Fit models using an In- or Sn-shell were clearly superior to those using exclusively Cu-shells (see Figure 7e and SI for details), indicating the formation of Cu-In or Cu-Sn intermetallic phases. The best fitting model and corresponding parameters are shown in Figure S21 and Table S9. The bulk ratios (Figures S26d-S27d) for the Cu-poor samples, however, are not in accordance with XPS, EDX, or ICP-OES, as for all samples – irrespective of element choice (M: In or Sn), suggested ratios (Cu-poor or -rich), or electrochemical treatment (as-prepared or reduced) – Cu:M atomic ratios of 1.5-9 are obtained in EXAFS, i.e., 10-40% is In or Sn. The discrepancy might stem from the fact that Cu-EXAFS only "detects" In or Sn being incorporated into the Cu-phase (by means of successful modeling), but is "blind" against a separate M(Ox) phase, whereas EDX and ICP-OES does not discriminate between phases (while XPS is surface-sensitive) and points towards a thermodynamic preferred mixture with low In or Sn amounts. Combining all techniques, one may argue for a core-shell structure with CuM-cores covered by M(Ox)-shells. There is an indication for Sn-enrichment in the course of electrochemical operation (from about 10% Sn before to 20-40% after operation), suggesting that parts of the reduced Sn atoms will be embedded into the Cu-Sn (core) structure. Figures 7f and S20 display Cu-EXAFS for all samples in FT-representation, showing large peaks for Cu-In samples and systematically lower peaks for the Cu-Sn samples, suggesting a considerable degree of crystallinity in the former and the lack of such in the latter. This is supported by the fact that not only the absolute peak heights are larger for Cu-In, but also that the ratio between the fourth peak at about 4.8 Å reduced distance and the first-shell peak at about 2.2 Å is larger for Cu-In than for Cu-Sn, indicating long-range order, see Figure 7f. Accordingly, EXAFS models including multiple-scattering shells were superior in describing Cu-In, but inferior in describing Cu-Sn. Figures 7f, Figure S19c, and S20c show that the degree of crystallinity is increasing with increasing amounts of In in Cu-In as well as with increasing potential due to In-enrichment. The latter effect is also partially visible in the Cu-Sn spectra. The first Cu-shell populations (NCu1) support those findings, in that they are highest in average for pure Cu foams (10.1), medium for Cu-In foams (8.7), and lowest for Cu-Sn foams (4.9), see also Table S11. With the exception of Cu rich In, In- and Sn-shell populations tend to rise after application of reductive potential (suggesting element incorporation), and notably, also the Cu–In and Cu–Sn distances ($R_{In/Sn}$) become shorter by 0.03-0.1 Å.

In summary, XAS reveals evidence for the formation of Cu-In or Cu-Sn alloy/intermetallic phases, containing 10-40% In or Sn. There are no indications for Cu oxide phase in the bulk material. In addition, separate $In(O_x)$ or $Sn(O_x)$ phases are always detected in the as-prepared materials. These oxidic phases get (partially) reduced and parts of the In or Sn atoms are likely incorporated into the Cu-In or Cu-Sn alloy during operation at catalytic potentials. The metallic Cu-In phase exhibits a considerable degree of crystallinity, which is not observed for the Cu-Sn phase.

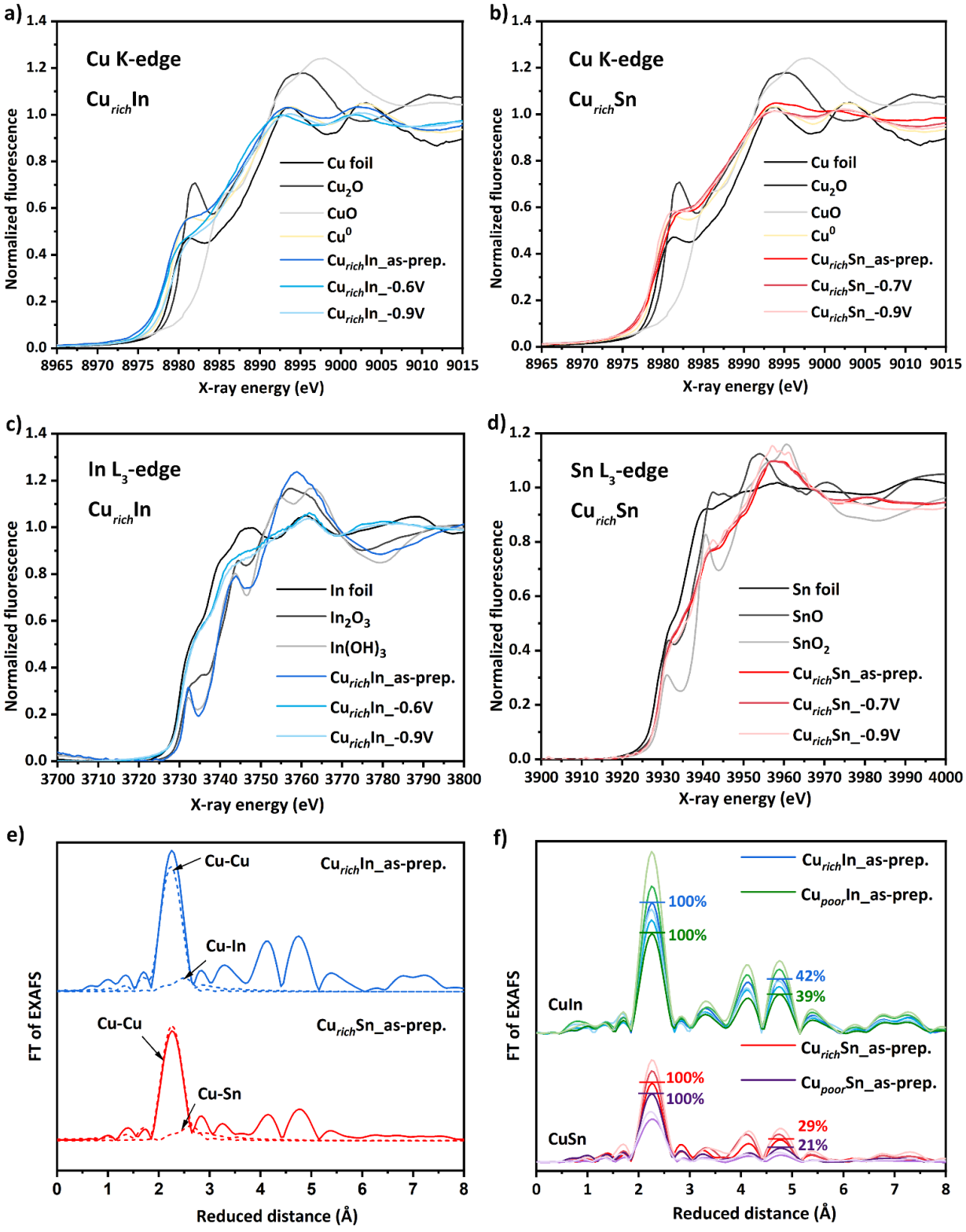

Figure 7. XAS analysis of Cu-In and Cu-Sn foams. (a) and (b) XANES at Cu K-edge for Cu rich Cu-In and Cu-Sn foams under different electrochemical conditions, see inset legends. (c) and (d) corresponding XANES at the In and Sn L_3-edges. (e) FT of EXAFS (Cu K-edge) for as-prepared samples of Cu rich CuIn and CuSn foam; contributions of first Cu-shell and In- or Sn-shell are highlighted by dashed lines. (f) FT of EXAFS (Cu K-edge) for all Cu-In (upper spectra) and Cu-Sn (lower spectra) foams; percentage numbers highlight the relative size of the first peak to the fourth peak for the as-prepared samples to convey different degrees of long-range order. Light blue/green/red/purple colors refer to samples after application of reductive potentials, see SI for details.

In-situ surface enhanced Raman spectroscopy

To obtain further dynamic information about adsorbed intermediates, local pH, and catalyst surface structure during CO_2ER, we studied the materials by *in situ* SERS. The results for the CO and $HCOO^-$ selective bimetallic foams are summarized in **Figures 8-9 and S28-30.** Under OCP (open circuit potential) and dry conditions, all the investigated catalyst materials including the bimetallic foams showed two strong peaks located at ~522-527 and ~619-623 cm^{-1}.[28] We measured Raman spectra of different Cu oxide/hydroxide standards (e.g., Cu_2O, CuO, $Cu(OH)_2$) for comparison, see Figure S28. Since these two aforementioned peaks do not perfectly match with any of the single oxide/hydroxide standards, we attribute them to a mixture of Cu_2O and CuO with Cu_2O as dominant surface species, which is in a good alignment with the obtained XPS results. For *in-situ* measurements (see the experimental section for more details), the as-prepared catalyst materials are first pre-activated (reduced) by applying constant cathodic current of -2 mA cm^{-2} in CO_2-saturated solution of 0.1 M $KHCO_3$ until reaching -0.4 V. Then, a constant potential of interest is applied for 2 hours to replicate relevant CO_2ER conditions. Interestingly, Cu-In bimetallic foams exhibited different activation-reduction behavior compared to the Cu-Sn bimetallic foams. The initial Cu_2O/CuO surface oxides of the as-prepared Cu-In bimetallic foams seem to be dynamically reduced with near-instantaneous formation of basic copper carbonate phase (metastable malachite/azurite like materials, $Cu_2CO_3(OH)_2$/$Cu_3(CO_3)_2(OH)_2$),[29] indicated by observation of vanishing Cu_2O/CuO peaks at 525 and 620 cm^{-1} and the immediate appearance of several new peaks assigned for malachite/azurite phases, as shown in **Figure 8a and Figure 9a**. On the other hand, the Cu_2O/CuO peaks (at 514-527 and 620 cm^{-1}) of the as-synthesized Cu-Sn bimetallic foams are not fading away during the pre-activation step, but rather they evolve into a one very strong peak at 585 cm^{-1}, which completely disappears within 10 minutes of the pre-activation step, as shown in **Figure 8b and 9b**.

The pure Cu and bimetallic foams exhibited several peaks between 411 cm^{-1} and 5240 cm^{-1} under CO_2 electrolysis at all investigated potentials. These peaks could be assigned to either a single or a mixture of Cu oxide/(oxy)hydroxide surface species. For example, $Cu_{85}In_{15}$ (CO selective) and $Cu_{25}In_{75}$ ($HCOO^-$ selective) exhibited a strong peak (at 530-536 cm^{-1}) combined with pre-shoulder peak (at 455-467 cm^{-1}) under CO_2 electrolysis at all the studied potentials (between -0.4 V and -0.9 V). These two peaks could be attributed to a mixture of $Cu(OH)_2$ and basic Cu carbonate ($Cu_x(CO_3)_y(OH)_z$, malachite/azurite) phases, since their positions match some of the obtained peaks for our internal measured $Cu(OH)_2$ and malachite standards. Additionally, the pure Cu foam exhibited a strong peak at 498 cm^{-1} with a pre-shoulder peak at 461 cm^{-1}, which can be attributed to $Cu(OH)_2$ based on alignment with that standard. Moreover, $Cu_{85}Sn_{15}$ (CO-selective) and $Cu_{40}Sn_{60}$ ($HCOO^-$-selective) also showed a strong peak at 597-598 cm^{-1} assigned to $Cu(OH)_2$. $Cu_{40}Sn_{60}$ showed additional peaks that can be assigned for malachite/azurite, as shown in **Figure 9b**. We will refer to the all observed peaks between 400 cm^{-1} and 630 cm^{-1} as mixture of copper (oxy)hydroxide and carbonate, species, since the obtained peaks in this region for our synthesized Cu-based bimetallic foams exhibited broad peaks compared to the measured Cu standards (see **Figure S28**). Indeed, the obtained operando SERS results provide evidence for the persistence of copper oxide surface species and their *in-situ* formation and transformation under CO_2 electrolysis conditions. Important to note is that in the absence of CO_2, neither of these peaks assigned to surface copper (oxy)hydroxide/carbonate species were observed. This highlights the essential role of the local environment changes developed during CO_2 electrolysis, such as local pH increase, on the dynamic transformation of Cu_2O/CuO of the as-prepared catalysts into $Cu_x(CO_3)_y(OH)_z$ under CO_2 electrolysis conditions. That is, the surface Cu_2O/CuO of the as-prepared samples *in-situ* converted into a mixture of Cu hydroxide ($Cu(OH)_2$) and basic Cu carbonate (malachite/azurite) during CO_2 electrolysis. The equilibrium between these two copper surface species are strongly dependent on the developed local environmental changes under CO_2 electrolysis. It is worth mentioning here that there are no peaks were identified to either In or Sn oxides under the applied measurement conditions.

The bicarbonate/carbonate (HCO_3^-/CO_3^{2-}) equilibrium was studied using operando SERS to quantify the induced local alkalization which occurs under CO_2 electrolysis conditions. The HCO_3^-/CO_3^{2-} equilibrium shifts towards CO_3^{2-} with the increase of pH,[27] resulting in a decrease of the intensity of HCO_3^- Raman bands (at 1018 cm^{-1} and 1365 cm^{-1}) and simultaneous increase of CO_3^{2-} band (at 1066 cm^{-1}). As shown in **Figure S29**, the intensity of this CO_3^{2-} band grew with the applying more negative potentials, especially for pure Cu foam. For instance, Cu foam local pH shifted from 6.8 at OCP into ~11 at -0.7 V, while the local pH of CO-selective bimetallic foams rose to 9.0 at same potential, providing direct evidence of the local alkalization developed under CO_2 electrolysis. Furthermore, $HCOO^-$ selective bimetallic foams also showed a local alkalization under CO_2 electrolysis, especially at higher applied potentials.

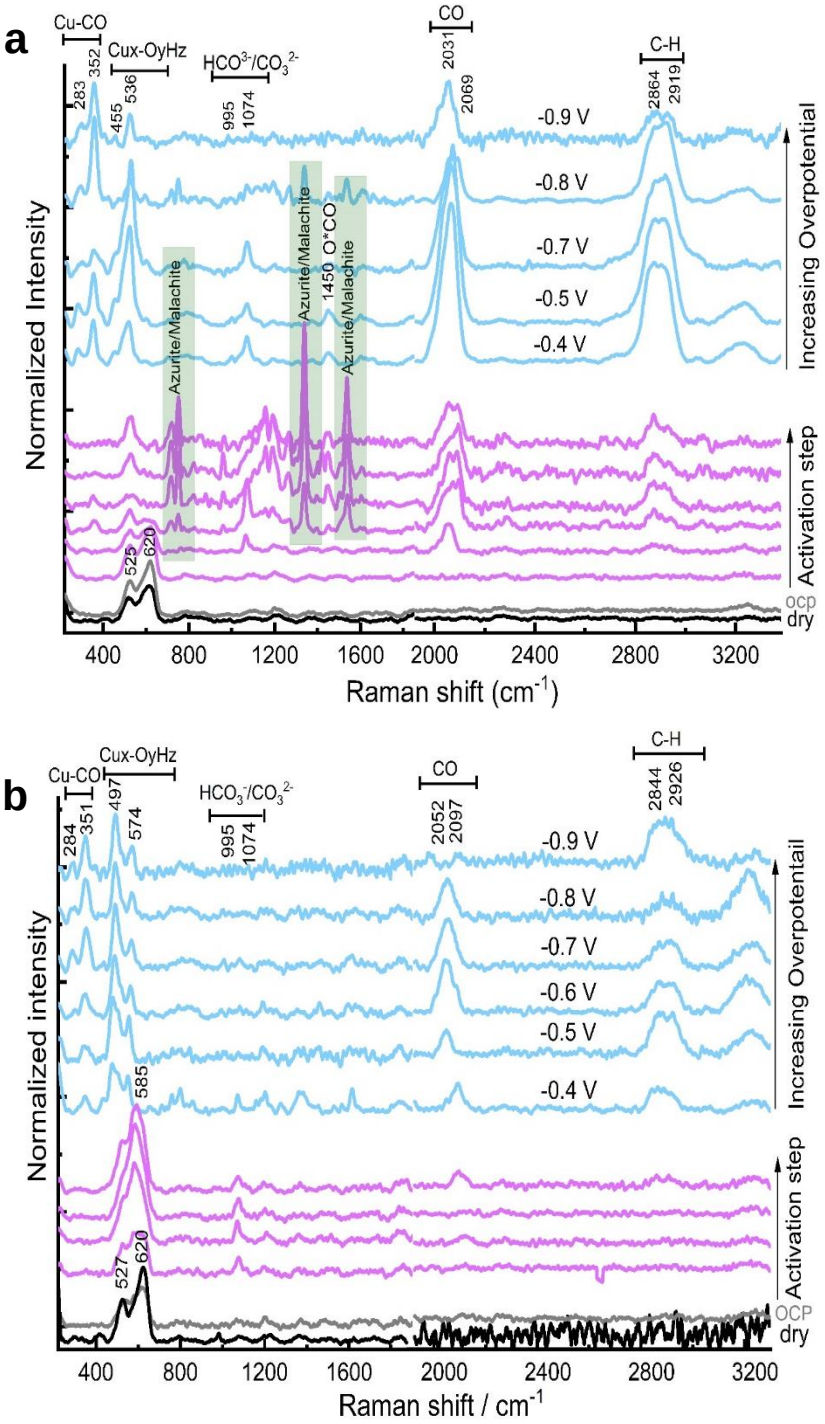

Figure 8. *In-situ* SERS obtained at CO-selective bimetallic foams; namely, $Cu_{85}In_{15}$ (a) and $Cu_{85}Sn_{15}$ (b) during the activation step (applying -2mA/cm^2 for 15 minutes) and at various applied potentials (from -0.4 V to -0.9 V) in CO_2-saturated 0.1 M $KHCO_3$.

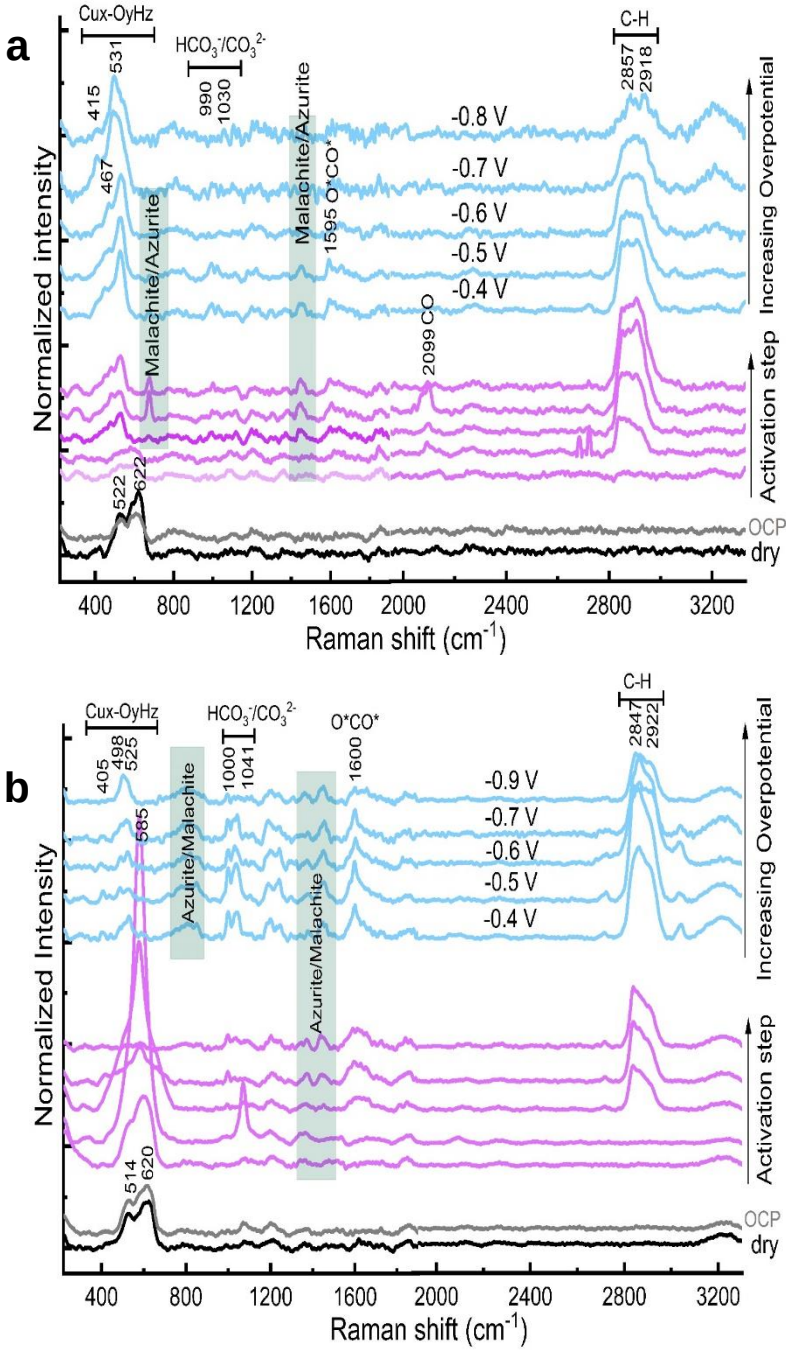

Figure 9. *In-situ* SERS obtained at CO-selective bimetallic foams; namely, $Cu_{25}In_{75}$ (a) and $Cu_{40}Sn_{60}$ (b) during the activation step (applying -2mA/cm^2 for 15 minutes) and at various applied potentials (from -0.4 V to -0.9 V) in CO_2-saturated 0.1 M $KHCO_3$.

Based on these observations, we were curious why these Cu hydroxide/carbonate surface species did not appear in our *quasi in-situ* glovebox-assisted XPS and XAS analyses. The main difference here is that the Raman spectra are acquired during continuous applied bias. Thus, we investigated the effects of bias removal on these detected Cu hydroxide/carbonate peaks to evaluate the possibility of surface transformation at open circuit in the electrolyte. We followed the induced changes in the obtained Raman spectra of our synthesized bimetallic foams over time following the bias removal, while either keeping them inside the same electrolyte or exposing them to air. As seen in **Figure S30**, the typical Cu_2O/CuO mixture peaks were observed along with

the complete disappearance of $Cu_x(CO_3)_y(OH)_z$ peaks for all investigated catalyst materials after taking them out of the electrolyte even for short time (<5 min). On the other hand, while remaining immersed these *in-situ* formed $Cu_x(CO_3)_y(OH)_z$ phases formed during CO_2 electrolysis stay observable for some time (15-25 minutes) after the bias removal. After that time, the equilibrium between $Cu(OH)_2$ and basic copper carbonate (malachite/azurite) shifts towards basic copper carbonate with time, as demonstrated by the appearance of several new peaks which can be assigned to malachite/azurite phases. We therefore conclude that while our *quasi in-situ XPS* approach does prevent the re-oxidation of catalyst surfaces after bias removal, it couldn't observe the Cu hydroxide/basic carbonate surface species since the presence of the local alkalization is essential for the stability of those phases. Both of the two CO selective bimetallic systems ($Cu_{85}In_{15}$ and $Cu_{85}Sn_{15}$) showed a similar CO selectivity, despite showing significant differences from each other in the dominant copper active-surface species. Even the pure copper foam showed a similar surface Cu species to the $Cu_{85}In_{15}$ (CO selective). Thus, we do not find any clear relationship between these observed Cu hydroxide/carbonate surface species and the CO_2ER to either CO or $HCOO^-$ of the different investigated catalyst materials.

The presence of adsorbed *CO on the surface of pure Cu and CO-selective bimetallic ($Cu_{85}In_{15}$ and $Cu_{85}Sn_{15}$) foams is evidenced by the presence of Raman peaks at ~280-284 cm^{-1}, 350-360 cm^{-1} and 1970-2070 cm^{-1}, assigned to the frustrated CO rotational mode (P1), Cu-CO stretching (P2) and intramolecular C≡O stretching, respectively (**Figure 8**).[30] P2 and P1 Raman bands usually indicate the interaction between the CO-intermediate and Cu surface. The intensity ratio of P2 and P1 Raman peaks (P2/P1) can be used to assess the *CO surface coverage at the solid-liquid interface during CO_2 electrolysis, with the ratio and *CO coverage scaling together.[30] As seen in Figure 8, CO-selective bimetallic foams ($Cu_{85}In_{15}$ and $Cu_{85}Sn_{15}$) exhibited a higher P2/P1 ratio compared to the pure Cu foam (Fig. S31), suggesting a higher *CO surface concentration at the bimetallic foams compared to the pure Cu foam, which correlates with higher FEs for CO evolution. On the other hand, neither of the CO-adsorption related peaks were observed for the $HCOO^-$-selective bimetallic foams ($Cu_{25}In_{75}$ and $Cu_{40}Sn_{60}$), which is expected since they are mainly $HCOO^-$ producers (**Figure 9**). Additionally, both exhibited a strong broad peak between at 2840-2950 cm^{-1} assigned for the C-H stretching (mainly $HCOO^-$) together with a well resolved peak at ~1595-1600 cm^{-1} attributed to the C-O stretching of the $HCOO^-$-pathway carboxylate intermediate (O-bound).

Schemes 1 and 2 summarize our observations of the surface-active species of CO- and $HCOO^-$-selective bimetallic catalysts (respectively), as evaluated from quasi *in-situ* XPS, and hypothesized general mechanisms of how the speciation relates to the observed selectivity switch from CO for Cu-rich to HCOO- for Cu-poor bimetallic catalysts. The enhanced CO production at Cu-rich system can be attributed to the localized partial negative charge on Cu sites due to the charge transfer from Sn/In atoms to Cu. This charge transfer from Sn/In into Cu led to partial positive charge on Sn atoms, indicated by the observing oxidized Sn and In species, and hence stabilizing the *COOH intermediate (CO-pathway).[17, 24]

4. Conclusions

Composition-tunable Cu-In and Cu-Sn bimetallic foams with dendritic nanomorphology were synthesized via a simple co-electrodeposition approach. Their compositions were tuned and optimized to achieve high CO_2 electroreduction selectively towards either $HCOO^-$ or CO. The selectivity of the prepared bimetallic foams towards CO_2ER strongly depends on the catalyst composition. The Cu-rich bimetallic foams (85% Cu, $Cu_{85}In_{15}$ and $Cu_{85}Sn_{15}$) showed a high CO-selectivity, while the Cu-poor bimetallic foams (25-40% Cu, $Cu_{25}In_{75}$ and $Cu_{40}Sn_{60}$) showed a high $HCOO^-$-selectivity. Despite both Cu-Sn and Cu-In bimetallic systems showing a similar CO_2ER dependency on the surface composition (Cu/Sn and Cu/In surface ratios), these bimetallic electrocatalysts showed significant differences in their surface speciation and CO_2ER enhancing mechanisms. Specifically, the indium and tin surface speciation are strongly dependent on the composition and the applied potentials. The surface of HCOO-selective bimetallic foams ($Cu_{40}Sn_{60}$ and $Cu_{25}In_{75}$) exhibited exclusively metallic surface species (Cu^0, Sn^0 and In^0) at potential with the highest $HCOO^-$ selectivity (-0.9 V), however they found to enhance the $HCOO^-$ pathway via different mechanisms. $Cu_{40}Sn_{60}$ enhances the $HCOO^-$ selectivity at the expense of the parasitic hydrogen evolution reaction, while $Cu_{25}In_{75}$ improves $HCOO^-$ production at the expense of CO.

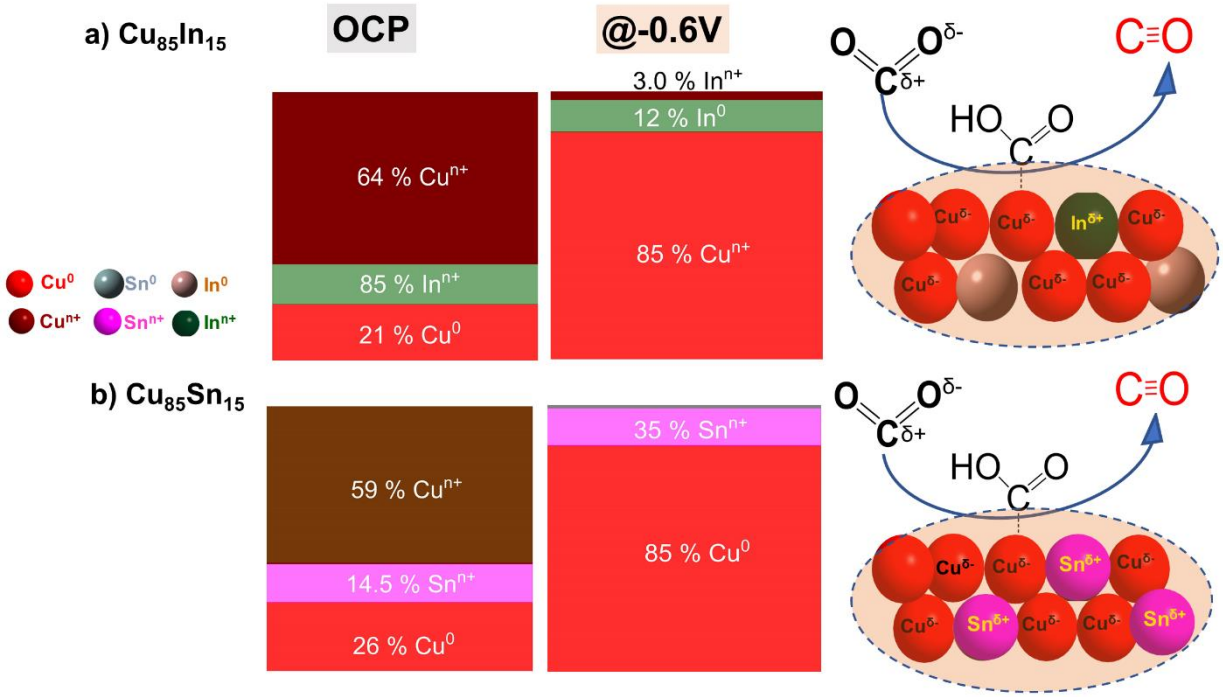

Scheme 1: schematic diagram showing the surface-active sites of CO-selective bimetallic catalysts and the role of these speciation in enhancing CO-pathway.

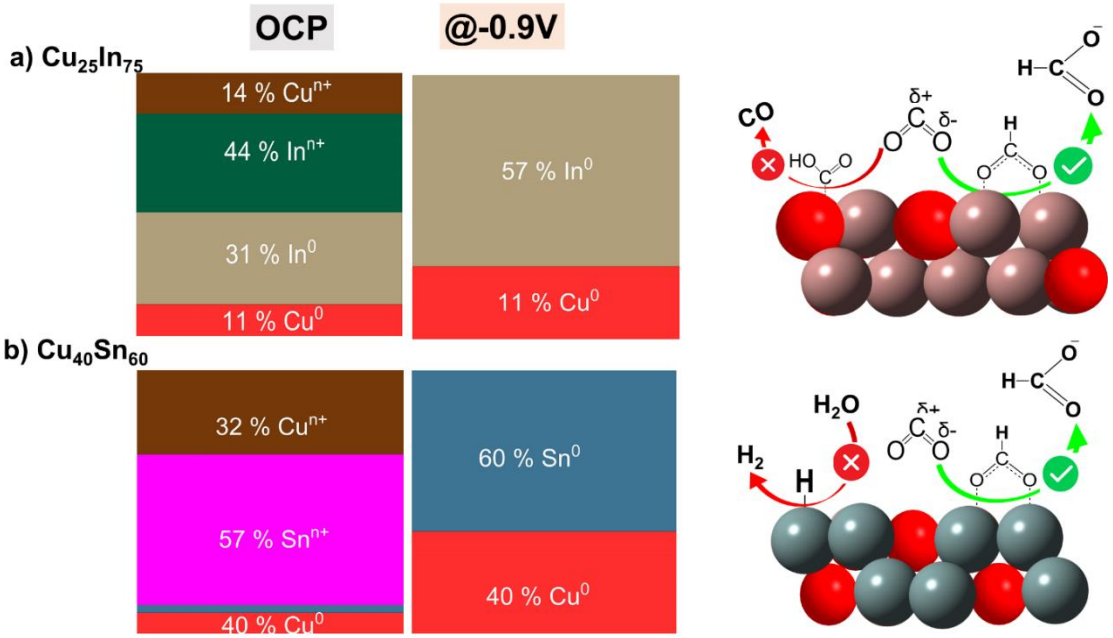

Scheme 2: schematic diagram showing the surface-active sites of $HCOO^-$-selective bimetallic catalysts and the role of these speciation in enhancing $HCOO^-$ pathway.

At all potentials below –0.9 V, 80% of the surface indium of $Cu_{25}In_{75}$ exists as metallic In (In^0) with low contribution of oxidized indium species, while under same conditions the surface speciation of $Cu_{40}Sn_{60}$ (HCOO-selective) showed that ~52% of the surface tin persists as oxidized tin species. This may explain the observed differences in their CO_2-performance at low potentials, where $Cu_{40}Sn_{60}$ mainly produces H_2, while $Cu_{25}In_{75}$ showed a high tendency for CO-formation under similar conditions. On the other hand, CO-selective bimetallic

foams (Cu-rich), $Cu_{85}In_{15}$ and $Cu_{85}Sn_{15}$, exhibited a similar CO2ER behavior, despite the significant differences of their surface speciation. $Cu_{85}In_{15}$ (CO-selective) exhibited the optimal CO-selectivity at –0.6 V, while $Cu_{85}Sn_{15}$ showed the same CO-selectivity (90%) at slightly higher potential (-0.7 V). The surface speciation of $Cu_{85}In_{15}$ showed that its surface mainly composed of metallic Cu and metallic In with low contribution of oxidized In species, while the surface of $Cu_{85}Sn_{15}$ was found to compose of metallic Cu and oxidized Sn species with a very low contribution of metallic Sn.

Despite the quasi *in-situ* XPS and XAS results indicating the full reduction of Cu under all the applied potentials, operando surface enhanced Raman spectroscopy measurements indicate the formation of a thin surface layer of $Cu(OH)_2$/malachite mixture during CO_2 electrolysis for all the studied catalyst materials (pure Cu and bimetallic foams). The $Cu(OH)_2$/malachite equilibrium depends on the local alkalinity developed under CO_2 electrolysis conditions. Operando SERS enables us to follow the transformation of the copper surface oxides into metallic copper and then into mixture of $Cu(OH)_2$/malachite during the activation step (applying -2 mA/cm^2). The SERS analysis provides direct evidence for the alkalinity developed under CO_2 electrolysis, where the local pH for the pure Cu foam and the CO-selective bimetallic foams rises from 7-8 to 10-11 during the first 10 minutes of CO_2 electrolysis. Operando SERS of the CO-selective bimetallic foams showed strong peaks for the CO intermediates, besides both of the CO-selective foams showed higher CO surface coverage compared to the pure Cu foams. On the other hand, the $HCOO^-$-selective bimetallic catalysts showed only peaks related to the formate-pathway (no peaks for CO-pathway were detected) which agree well with the observed CO_2ER performance.

In summary, the complementary information gained from the various spectroscopic and microscopic techniques in ex-, quasi *in-situ* or operando approaches allows us to fully examine the origin of the selectivity switch for the bimetallic Cu-M (M=In or Sn) catalysts from CO to $HCOO^-$ upon increasing In or Sn contents. The information gathered from these techniques enabled us to understand the significant differences in the surface speciation and composition of between Cu-In and Cu-Sn systems, despite both systems showing similar CO_2ER performance. Our findings from *in-situ* SERS highlight the importance of the developed local alkalinity in the formation of oxidized surface Cu species, where a mixture of Cu hydroxide and basic Cu carbonate (metastable malachite like materials) was observed.

Supporting Information

The detailed information of the utilized materials, chemicals and techniques; synthesis procedures of various Cu-Sn and Cu-In catalysts; additional morphological, structural and compositional characterization figures for the studied catalysts including SEM, XRD, XPS and elemental mapping; details of EXAFS fit models and parameters; additional electrochemical, *in-situ* Raman and quasi *in-situ* XAS data.

Acknowledgments

This work was supported by the European Union's Horizon 2020 research and innovation program (FlowPhotoChem project, grant 862453) and the Helmholtz Association's Initiative and Networking Fund (Helmholtz Young Investigator Group VH-NG-1225). This study used instrumentation provided by the Helmholtz Energy Materials Foundry (HEMF) laboratories and the HZB Institute for Solar Fuels. The authors wish to thank Christian Höhn, René Gunder and Holger Kropf for experimental support. H.D., M.S. and F.Y. were funded by the Deutsche Forschungsgemeinschaft (DFG, German Research Foundation) under Germany's Excellence Strategy – EXC 2008/1 – 390540038 – UniSysCat, by the DFG as project DA 402/9-1, and by the German Federal Ministry of Education and Research (BMBF project "Operando XAS"). F.Y. gratefully acknowledge support by the China Scholarship Council (CSC) in form of a doctoral fellowship. We thank Prof. Dr. Christina Roth (Bayreuth) for supporting discussions. X-ray absorption spectroscopy (XAS) was performed at beamline KMC-3 of the BESSY synchrotron (Berlin-Adlershof) operated by the Helmholtz-Zentrum Berlin (HZB); we thank the staff at BESSY/HZB and various researchers from Freie Univ. Berlin (FUB) for support in data collection, especially Drs. Michael Haumann (XAS), Paul Beyer (XAS) and Shan Jiang (Raman spectroscopy).

References

1. C. Chen, J. F. Khosrowabadi Kotyk and S. W. Sheehan, *Chem*, 2018, **4**, 2571-2586.
2. O. S. Bushuyev, P. De Luna, C. T. Dinh, L. Tao, G. Saur, J. van de Lagemaat, S. O. Kelley and E. H. Sargent, *Joule*, 2018, **2**, 825-832.
3. H. Shin, K. U. Hansen and F. Jiao, *Nature Sustainability*, 2021, **4**, 911-919.
4. S. Alinejad, J. Quinson, G. K. H. Wiberg, N. Schlegel, D. Zhang, Y. Li, S. Reichenberger, S. Barcikowski and M. Arenz, *ChemElectroChem*, 2022, **9**, e202200341.
5. A. de Klerk, in *Kirk‐Othmer Encyclopedia of Chemical Technology*, DOI: https://doi.org/10.1002/0471238961.fiscdekl.a01, pp. 1-20.
6. K. P. Kuhl, E. R. Cave, D. N. Abram and T. F. Jaramillo, *Energy & Environmental Science*, 2012, **5**, 7050-7059.
7. Z. Ma, U. Legrand, E. Pahija, J. R. Tavares and D. C. Boffito, *Industrial & Engineering Chemistry Research*, 2021, **60**, 803-815.
8. F. Muench, G. A. El-Nagar, T. Tichter, A. Zintler, U. Kunz, L. Molina-Luna, V. Sikolenko, C. Pasquini, I. Lauermann and C. Roth, *ACS Applied Materials & Interfaces*, 2019, **11**, 43081-43092.
9. S. Stojkovikj, G. A. El-Nagar, F. Firschke, L. C. Pardo Pérez, L. Choubrac, M. Najdoski and M. T. Mayer, *ACS Applied Materials & Interfaces*, 2021, **13**, 38161-38169.
10. A. Bagger, W. Ju, A. S. Varela, P. Strasser and J. Rossmeisl, *ChemPhysChem*, 2017, **18**, 3266-3273.
11. S. Nitopi, E. Bertheussen, S. B. Scott, X. Liu, A. K. Engstfeld, S. Horch, B. Seger, I. E. L. Stephens, K. Chan, C. Hahn, J. K. Nørskov, T. F. Jaramillo and I. Chorkendorff, *Chemical Reviews*, 2019, **119**, 7610-7672.
12. P. Grosse, D. Gao, F. Scholten, I. Sinev, H. Mistry and B. Roldan Cuenya, *Angewandte Chemie International Edition*, 2018, **57**, 6192-6197.
13. Y. Li, F. Cui, M. B. Ross, D. Kim, Y. Sun and P. Yang, *Nano Letters*, 2017, **17**, 1312-1317.
14. F. Scholten, I. Sinev, M. Bernal and B. Roldan Cuenya, *ACS Catalysis*, 2019, **9**, 5496-5502.
15. A. Vasileff, C. Xu, Y. Jiao, Y. Zheng and S.-Z. Qiao, *Chem*, 2018, **4**, 1809-1831.
16. T. Kottakkat, K. Klingan, S. Jiang, Z. P. Jovanov, V. H. Davies, G. A. M. El-Nagar, H. Dau and C. Roth, *ACS Applied Materials & Interfaces*, 2019, **11**, 14734-14744.
17. L. C. Pardo Pérez, A. Arndt, S. Stojkovikj, I. Y. Ahmet, J. T. Arens, F. Dattila, R. Wendt, A. Guilherme Buzanich, M. Radtke, V. Davies, K. Höflich, E. Köhnen, P. Tockhorn, R. Golnak, J. Xiao, G. Schuck, M. Wollgarten, N. López and M. T. Mayer, *Advanced Energy Materials*, 2022, **12**, 2103328.
18. M. Zhu, P. Tian, J. Li, J. Chen, J. Xu and Y.-F. Han, *ChemSusChem*, 2019, **12**, 3955-3959.
19. W. Luo, W. Xie, R. Mutschler, E. Oveisi, G. L. De Gregorio, R. Buonsanti and A. Züttel, *ACS Catalysis*, 2018, **8**, 6571-6581.
20. S. Rasul, D. H. Anjum, A. Jedidi, Y. Minenkov, L. Cavallo and K. Takanabe, *Angewandte Chemie International Edition*, 2015, **54**, 2146-2150.
21. M. Rahaman, K. Kiran, I. Zelocualtecatl Montiel, A. Dutta and P. Broekmann, *ACS Applied Materials & Interfaces*, 2021, **13**, 35677-35688.
22. X. Hou, Y. Cai, D. Zhang, L. Li, X. Zhang, Z. Zhu, L. Peng, Y. Liu and J. Qiao, *Journal of Materials Chemistry A*, 2019, **7**, 3197-3205.
23. Q. Li, J. Fu, W. Zhu, Z. Chen, B. Shen, L. Wu, Z. Xi, T. Wang, G. Lu, J.-j. Zhu and S. Sun, *Journal of the American Chemical Society*, 2017, **139**, 4290-4293.
24. A. Vasileff, X. Zhi, C. Xu, L. Ge, Y. Jiao, Y. Zheng and S.-Z. Qiao, *ACS Catalysis*, 2019, **9**, 9411-9417.
25. A. Jedidi, S. Rasul, D. Masih, L. Cavallo and K. Takanabe, *Journal of Materials Chemistry A*, 2015, **3**, 19085-19092.
26. M. Görlin, P. Chernev, J. Ferreira de Araújo, T. Reier, S. Dresp, B. Paul, R. Krähnert, H. Dau and P. Strasser, *Journal of the American Chemical Society*, 2016, **138**, 5603-5614.
27. K. Klingan, T. Kottakkat, Z. P. Jovanov, S. Jiang, C. Pasquini, F. Scholten, P. Kubella, A. Bergmann, B. Roldan Cuenya, C. Roth and H. Dau, *ChemSusChem*, 2018, **11**, 3449-3459.
28. S. Jiang, K. Klingan, C. Pasquini and H. Dau, *The Journal of Chemical Physics*, 2019, **150**, 041718.
29. S. Jiang, L. D'Amario and H. Dau, *ChemSusChem*, 2022, **15**, e202102506.

30. C. Zhan, F. Dattila, C. Rettenmaier, A. Bergmann, S. Kühl, R. García-Muelas, N. López and B. R. Cuenya, *ACS Catalysis*, 2021, **11**, 7694-7701.